

Article

# Water–Rock Interaction Processes in Tíscar and Larva Active Faults (Betic Cordillera, SE Spain)

Rosario Jiménez-Espinosa \* , Pilar Hernández-Puentes and Juan Jiménez-Millán 

Departamento de Geología and Centro de Estudios Avanzados en Ciencias de la Tierra, Energía y Medio Ambiente (CEACTEMA), Campus Las Lagunillas, University of Jaén, 23071 Jaén, Spain; pili.puentes@gmail.com (P.H.-P.); jmillan@ujaen.es (J.J.-M.)

\* Correspondence: respino@ujaen.es

**Abstract:** A hydrochemical and mineral study of groundwaters and damaged rocks from the Tíscar and Larva fault zones (Betic Cordillera, Iberian Peninsula) was carried out in order to (a) describe the physical and chemical properties of the groundwaters; (b) recognize significant locations with deep-origin fluids related to active tectonics; (c) and to describe the water–rock interaction and the neoformation of clay mineral processes and their importance in the seismicity of the faults. A sampling campaign was completed between November 2012 and November 2013, during which data were obtained from 23 different groundwater sites in the fault areas. Two main groups of waters were distinguished: (a)  $\text{Ca}^{2+}$ - $\text{Mg}^{2+}$ - $\text{HCO}_3^-$  facies characterized by poor conductivity and salinity; and (b) saline waters (up to 30 meq/L) rich in  $\text{Ca}^{2+}$ - $\text{Mg}^{2+}$ - $\text{SO}_4^{2-}$ - $\text{Cl}^-$  and with an elevated conductivity (frequently  $> 1000 \mu\text{S}/\text{cm}$ ). In addition, a minor group of saline and warm waters ( $T > 16.5^\circ\text{C}$ ) was found to be  $\text{Na}^+$ -rich and show moderately high B values ( $> 0.33 \text{ ppm}$ ), and which might be hosted in aquifers deeper than the two main groups. This group of deep-origin waters is oversaturated in clay minerals and is in equilibrium for Ca-Mg carbonate minerals. X-ray diffraction and scanning and transmission electron microscopy data corroborate the crystallization forecast of authigenic smectite, which appears as thin films coating carbonate fragments. The origin of smectite is related to the fragile strain and thermal–fluid–mineral interactions in fault rocks. Smectite could lubricate carbonate rocks, which favor creep deformation versus seismic slip. This work provides locations where groundwater physico-chemical properties and composition suggest tectonic fault activity.



**Citation:** Jiménez-Espinosa, R.; Hernández-Puentes, P.; Jiménez-Millán, J. Water–Rock Interaction Processes in Tíscar and Larva Active Faults (Betic Cordillera, SE Spain). *Water* **2024**, *16*, 897.

<https://doi.org/10.3390/w16060897>

Academic Editor: Ondra Sracek

Received: 26 February 2024

Revised: 14 March 2024

Accepted: 17 March 2024

Published: 20 March 2024



**Copyright:** © 2024 by the authors. Licensee MDPI, Basel, Switzerland. This article is an open access article distributed under the terms and conditions of the Creative Commons Attribution (CC BY) license (<https://creativecommons.org/licenses/by/4.0/>).

## 1. Introduction

Fault zones have the capacity to be hydraulic conduits connecting shallow and deep geological environments [1–3]. Mineral precipitations along fault zones are usually considered an indication of accentuated groundwater flow through faults, e.g., [4–6]. The crystallization of mineral phases in fault areas is controlled by the chemistry of circulating fluid, the characteristics of the fault rocks, and the physical factors present at the time of mineralization. The chemical composition of groundwater fluids circulating through active fault zones can be affected by geological processes, sometimes linked to the nucleation and propagation of earthquake processes that occur in these areas, such as (i) the discharge of water and other liquids produced by the consolidation or liquefaction of shallow sediments, see, e.g., [7]; (ii) dryness reactions of clay minerals in depth zones [8–11]; (iii) and dissolution–precipitation processes in rocks through which groundwater has passed, see, e.g., [12]. The spatio-temporal variations in groundwater hydrochemical constituents produced by these processes could be used in future studies on earthquake prediction [13]. Moreover, the fault zones favor substantial mixing between deep high-T waters and cold surficial waters that modify the physical–chemical groundwater parameters controlling the mineral stability.

Mineralization related to the flow of water and water–rock exchange could influence the mechanical strength of faults, e.g., [14]. The crystallization of low-friction minerals in fault gouges, such as clay minerals, plays a significant role in the dynamics of faults, generates typical deformation microstructures and is frequently related to stable creeping processes and aseismic slip [15].

The assessment of the influence of fluid flow patterns and fluid–rock interactions in fault zones remains a challenge and requires the integration of hydrogeological, geochemical, and mineralogical data. In this manuscript, a multidisciplinary study of the hydrogeology and mineralogy of fault zones is described to link the chemical signatures of deep groundwaters to the crystallization of neoformed minerals in fault sectors to expand on the current knowledge of the effect of fluid flow and water–rock interaction processes on the mechanical behavior of fault zones. The study area selected for this study is the Guadiana Menor valley (Betic Cordillera, SE Spain), characterized by several active structures such as the Tíscar and Larva faults. These zones have a significant seismic risk, as recently exemplified by the January 2012 earthquake (intensity IV and magnitude > 4) the epicenter of which was located at Huesa (north of Jaén province). Nevertheless, the seismicity in the zone is mostly characterized by low-to-moderate-magnitude earthquakes.

We report the chemical characteristics of waters taken from the Tíscar and Larva fault areas from springs and wells; groundwaters with different origins and circulations were sampled. We aimed to give a geochemical description of the fluids circulating over these active faults and a mineralogical characterization of their fault rocks in order to achieve the following:

- (a) Identify relevant sites with deep-origin waters that could be mobilized during seismic events to reach surficial areas along faults, allowing for the creation of a regional network to monitor groundwater geochemical variations related to fault activity.
- (b) Characterize the effect of the processes of water circulation and neoformation of clays associated with these fault zones to provide data that contribute to the understanding of the physical comportment of these rocks and its impact on the seismicity of the region.

## 2. Materials and Methods

### 2.1. Study Area: Geology and Hydrogeology Framework

The study zone is located in the External Zone of the Betic Cordillera, in the Prebetic domain, at latitude  $37^{\circ}45' - 37^{\circ}50'$  N and longitude  $3^{\circ} - 3^{\circ}05'$  W (Figure 1). This sector is located in the tectonic corridor of Guadiana Menor River [16,17]. Two major fault zones are described in the zone: Tíscar and Larva.

The main fault of the study area is the N130–150E Tíscar fault. This dextral fault, 20 km in length, has a total displacement of around 6 km. It deforms the Mesozoic and Tertiary sedimentary cover [18,19]. Next to the Guadiana Menor River there are several parallel fractures to the main Tíscar strand. In this wide deformation zone between Tíscar and the Guadiana Menor River there is a small N30E normal fault SE of Quesada, next to Acra, which deforms carbonate rocks. The thermal waters related to this fault have been studied previously [17,20–22].

There is a N90–120E strike-slip fault to the west of the Tíscar fault zone, the Larva fault. This structure deforms the Upper Miocene marls and marlstones and Oligocene calcarenites and bioclastic limestones. This is the seismogenic source of an earthquake with intensity V and magnitude 4.4 mD that occurred on 22 May 1951, with an aftershock in Peal de Becerro with intensity III and magnitude 3.4 mD [23].

The region is associated with significant seismic risk, as was recently revealed by a 4.4 mbLg (4.0 Mw) earthquake and 15 aftershocks that occurred in west of Huesa [24]. Table 1 shows the most relevant earthquakes recorded since 1951 with magnitude >2. In addition, more than 50 earthquakes with magnitude <2 have been recorded since 1951 in this region. In Table 2 physical–chemical parameters, major and minor elements, and isotopic composition of Tíscar–Larva fault zone aquifers are presented.

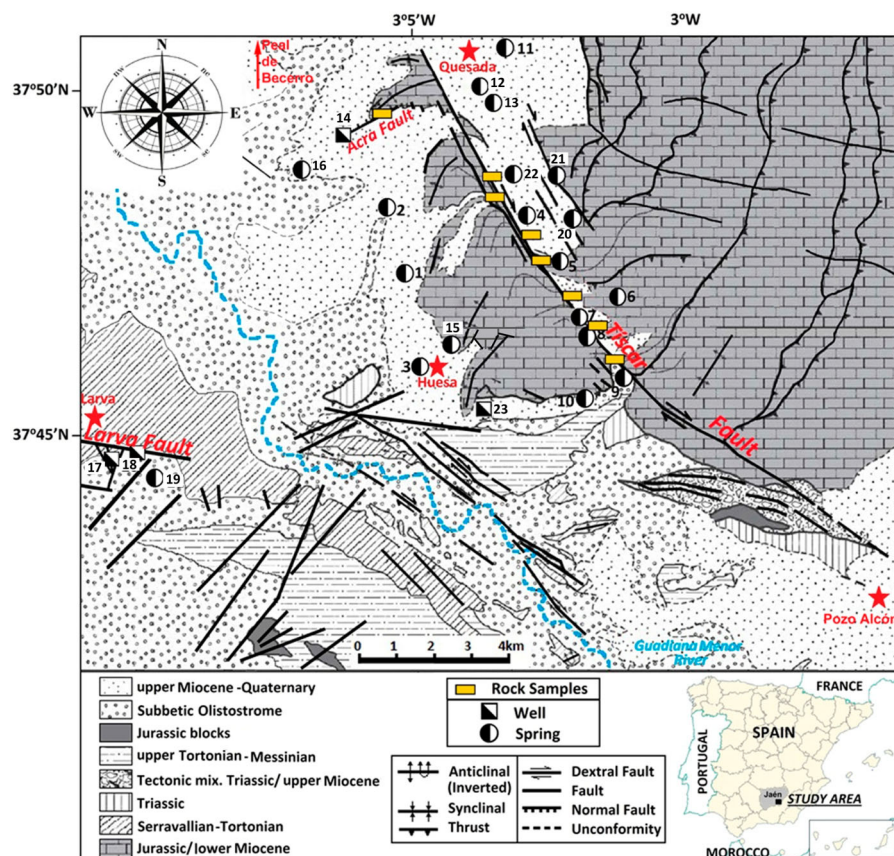


**Figure 1.** Geological setting of the study area (modified and extended from Foucault (1971) [18]). Numbers in the map indicate sampling locations for groundwater and rocks. Sample identification numbers refer to Table 2. Stars indicate location of main villages in the study area.

**Table 1.** History of seismic activity around the Tíscar–Larva fault zones since 1951.

Date	Intensity	Magnitude	Epicenter
22 May 1951	V	4.4	Larva
22 May 1951	III	3.4	Peal de Becerro
4 July 1958		3.5	Peal de Becerro
26 January 1994		2.9	S Larva
11 March 1994		2.8	NE Larva
4 October 1996		2.5	SE Larva
27 April 1998		3.1	SW Huesa
27 April 1998		2.0	W Huesa
4 May 1998		2.1	Peal de Becerro
4 November 2000		2.1	NE Larva
9 November 2000		2.3	NE Larva
9 November 2000		3.4	NE Larva
16 December 2001		2.1	NW Huesa
3 August 2003		2.0	NE Larva
2 December 2006		2.1	NE Larva
15 March 2010		2.4	NW Larva
21 April 2010		2.0	NE Pozo Alcón
31 January 2012		2.9	W Huesa
31 January 2012		4.0	W Huesa
31 January 2012		2.1	SW Quesada
1 February 2012		2.2	SW Quesada
1 February 2012		2.1	SW Quesada
18 September 2014		2.8	Peal de Becerro

**Table 2.** Physical–chemical parameters, major and minor elements, and isotopic composition of Tíscar–Larva fault zone aquifers.

Sample	E.C. (μS/cm)	T °C	pH	HCO <sub>3</sub> <sup>−</sup> mg/L	SO <sub>4</sub> <sup>2−</sup> mg/L	Cl <sup>−</sup> mg/L	NO <sub>3</sub> <sup>−</sup> mg/L	Na <sup>+</sup> mg/L	K <sup>+</sup> mg/L	Ca <sup>2+</sup> mg/L	Mg <sup>2+</sup> mg/L	Si mg/L	Al mg/L	B mg/L	<sup>3</sup> H UT
1	840	13.7	7.5	256.3	57.4	10.0	27.4	7.0	1.2	68.0	19.5	1	0.000	<0.05	
2	470	15.0	7.8	270.0	9.8	13.0	8.5	5.0	1.4	64.0	14.0	1	0.001	<0.05	
3	488	11.0	7.9	274.6	11.3	10.2	2.3	5.1	1.7	76.0	8.6	2	0.001	<0.20	
4	627	9.5	9.6	345.0	24.9	15.9	5.0	7.0	2.5	78.0	28.0	5	0.056	<0.20	
5	379	11.7	8.2	244.1	11.6	6.9	7.0	2.8	0.6	67.0	11.5	2.5	0.001	<0.05	
6	408	14.0	7.8	231.9	12.7	7.9	10.0	3.8	1.0	63.0	8.6	2	0.000	<0.10	
7	405	13.8	7.6	267.8	10.6	6.4	12.6	3.9	0.8	62.0	18.6	1	0.001	<0.20	
8	377	11.7	8.7	285.1	11.5	5.2	6.0	5.5	0.7	59.0	17.8	1	0.001	<0.10	
9	522	14.1	7.4	318.3	16.0	8.4	3.1	4.8	2.0	65.0	21.5	1	0.000	<0.05	
10	602	14.8	8.8	305.1	56.6	12.1	22.0	8.1	2.4	84.0	17.0	1	0.001	<0.05	
11	547	16.8	7.5	329.5	15.1	22.8	2.7	1.9	20.5	74.2	23.2	1	0.010	<0.05	
12	1372	14.4	9.4	366.1	352.2	41.6	113.7	25.0	17.0	172.9	66.2	5	0.014	0.33	
13	1035	15.3	8.1	353.9	91.7	39.9	138.8	7.5	29.8	103.9	40.9	5	0.013	0.83	
14	665	25.2	7.2	323.4	15.4	56.1	9.7	26.1	14.7	68.7	24.0	2.5	0.039		
15	650	17.6	8.1	366.1	26.9	18.9	13.3	8.7	13.4	54.4	45.8	2.5	0.016	0.54	
16	1311	20.0	7.5	476.0	81.6	155.9	34.4	70.0	15.5	110.3	61.5	7.5	0.009	0.34	
17	1817	25.0	7.1	183.1	527.1	206.9	9.7	127.9	5.7	155.9	89.9	2.5	0.027		
18	830	17.6	7.7	262.4	243.1	29.6		11.8	2.8	125.7	35.9	2.5	0.008		
19	509	16.0	7.5	280.7	17.1	24.9	11.9	9.1	1.8	95.3	7.0	1	0.007		
20	550	16.0	7.5	366.1	16.7	7.1	3.4	1.7	3.2	57.5	41.4	2.5	0.022		
21	724	17.0	7.6	390.0	50.0	12.1	25.0	8.1	1.5	80.0	34.6	5	0.015		
22	662	15.5	6.9	366.1	30.6	14.8	20.7	4.7	1.3	73.3	30.4	5	0.006		
23	411	15.0	6.7	279.6	19.2	8.0	2.8	4.5	1.6	51.8	24.5	1	0.010	4.05	

From a hydrogeological point of view, some major aquifers in the province of Jaén are located in this study area, with many natural springs that may have been affected by the earthquake in Huesa in 2012. They are mainly karst aquifers in Cretaceous dolostones and limestones here. Apart from the major carbonate aquifers, a number of permeable detrital formations can be found in the Guadiana Menor corridor (Figure 2). The main hydrogeological units are as follows [25,26]:

- (a) Alto Guadalquivir aquifers, which belong to different geological domains, representing the Prebetic Zone (external and internal), corresponding to the Sierra de Cazorla and Sierra de Segura and different Subbetic carbonate units.
- (b) Aquifers of Sierra del Pozo, within the bigger unit of the Sierra de Quesada-Castril aquifers, located entirely in the internal Prebetic Zone, matching the set of mountainous Sierra Segura units, aligned NNE-SSW. They have a permeable area of 800 km<sup>2</sup>, where towards the NE, hydrogeological continuity is established, while the W limits are set by Alto Guadalquivir, which contacts the impermeable base of the Triassic clays. The SW limit is arbitrary and, in the S and SE, the limits are set in the Mesozoic zone, the discordant edge of the Neogene–Quaternary zone under the Guadix Depression’s detrital deposits.

## 2.2. Methods

### Sampling and Analytical Procedures

Between November 2012 and November 2013, a total of 23 sampling points, wells and springs, were selected in the area. Major and minor elements were analyzed in these sites, as well as the radioactive isotope of hydrogen (tritium, <sup>3</sup>H) in a selection of sites. The physical and chemical variables measured in situ with a Hanna Instruments water quality meter (HI-9828) were electrical conductivity for a standard temperature of 25 °C (EC (μS/cm), ±1 μS/cm), total dissolved solids (TDS (ppm), ±1 ppm), pH (±0.02 pH), temperature (T) (°C, ±0.15 °C). Alkalinity was also determined by volumetric titration.

Different water samples were taken in high-density polyethylene bottles (HDPE), rinsed with groundwater. In one bottle, nitric acid (HNO<sub>3</sub>) was added to reduce the pH < 2.0 to stabilize metals. The samples were filtered through 0.45 μm membranes and deposited in ice boxes and transported to our laboratory and stored at 4 °C for analysis in different laboratories. The major elements were determined using a Metrohm 850 Professional Ion Chromatograph (Metrohm AG, Herisau, Switzerland) (Scientific Instrumentation

Centre, University of Jaén) with relative error of analysis of  $\pm 1\%$ . An Agilent Model 7500 ICP-mass spectrometer (Agilent, Santa Clara, CA, USA) (errors < 5% RSD, Scientific Instrumentation Centre, University of Jaén) was used for the obtention of metals and traces. The analysis of boron was performed in the Scada S.A. Laboratory in Granada with a UV-170 spectrophotometer using the azomethine colorimetric method (relative errors  $\pm 0.28$  to  $0.42\%$ ). AquaChem 2010.1 software (Schlumberger Water Services) and Phreeqc version 2 for Windows (USGS) were used to process the hydrochemical data.

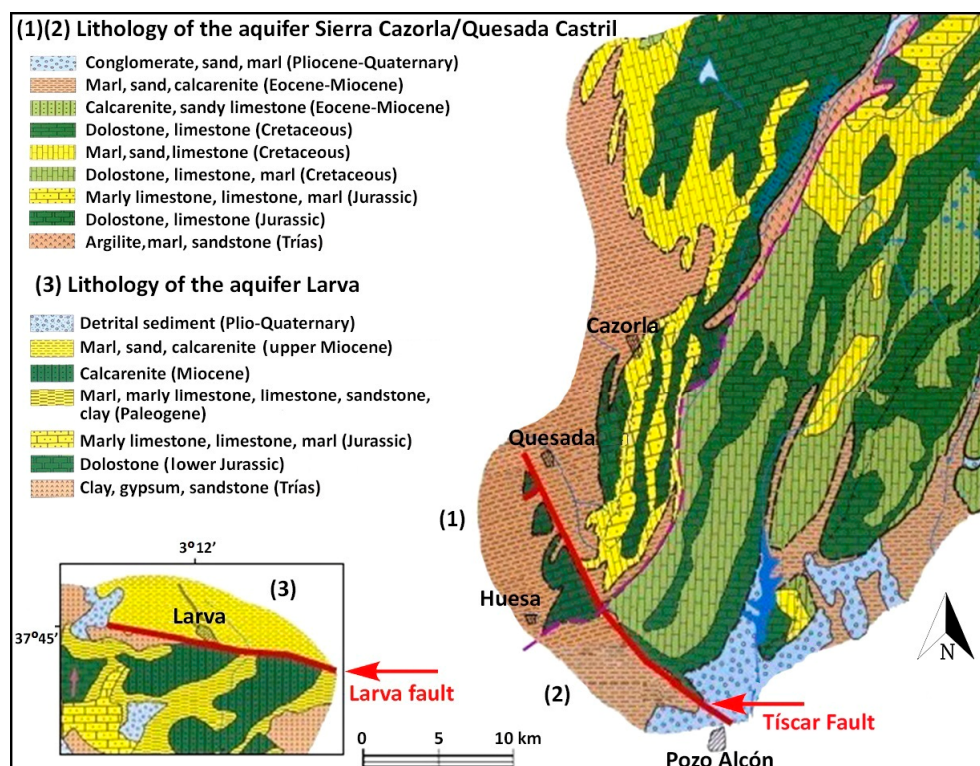


**Figure 2.** Main hydrogeological units of Tíscar–Larva fault zones (after [25,26] ITGE 1997; ITGE 1998).

Tritium ( ${}^3\text{H}$ ) was analyzed at the Scientific Instrumentation Centre (University of Granada) using a Beckman LS6500 scintillation counter (liquid scintillation Gold LLT, Perkin Elmer, Waltham, MA, USA). Errors were around  $\pm 5\%$ .

Eight samples of fault zones were taken for mineralogical characterization. Samples were crushed to obtain the powder for the analysis. The mineralogical composition was determined by X-ray diffraction (XRD) from random powders and oriented aggregates to achieve a better characterization of the clays. For this purpose, a PANalytical X'Pert Pro diffractometer (PANalytical, Eindhoven, The Netherlands) (Scientific Instrumentation Centre, University of Jaén, SIC, Spain) equipped with an X'Celerator solid-state linear detector using  $\text{CuK}\alpha$  radiation, 45 kV, 40 mA,  $0.008^\circ$   $2\theta$  step increment, and 10 s/step counting time was used. A dispersion on a glass slide was used to make the oriented aggregates, which were treated in several ways to identify the expandable minerals. They were analyzed after being air-dried, intercalated with ethylene glycol (subjected to saturated environment at  $70\text{ }^\circ\text{C}$  for 24 h), and heated at  $300\text{ }^\circ\text{C}$  for 1 h. HighScore Plus 5.1 software (PANalytical, Eindhoven, The Netherlands) was used for mineral identification.

A Carl Zeiss MERLIN high-resolution scanning electron microscope (FESEM) with EDX analytical capability (Carl Zeiss, Oberkochen, Germany) (SIC, University of Jaén, Spain) was used to obtain analytical and textural data through secondary electron (SE) imaging. For this purpose, sediment samples were mounted on supports and metallized with carbon. In addition, the backscattered electron (BSE) detector was used to complete the characterization of minerals with metallic content.

The nanometric characterization was carried out using high-resolution transmission electron microscopy (HRTEM) following the experimental procedure indicated by Nieto et al. [27]. For the compositional characterization of the clays, the grain size of which often escapes the resolution of the SEM, the HRTEM transmission electron microscope, HAADF FEI TITAN G2 microscope, operating at 300 kV, and the HRTEM HAADF Thermo Fisher TALOS operating at 200 kV were used (Scientific Instrumentation Centre, University of Granada). Chemical analyses of the nanoparticles were obtained from powders dispersed over gold or nickel grids in scanning transmission electron microscope mode with an energy-dispersive X-ray spectroscopy (AEM-EDX) microanalysis system (Thermo Fisher, Eindhoven, The Netherlands).

### 3. Results and Discussion

#### 3.1. Groundwater Chemistry

Table 2 displays the analytical results for the 23 studied groundwater samples and the tritium content of the 10 selected samples. These waters have low salinity values and pH ranging from 6.6 to 9.6, with the majority of samples displaying an alkaline trend, related to carbonate rocks. The discharge temperatures vary from 9.5 to 25.2, whereas the EC oscillates between 377 and 1817  $\mu\text{S}/\text{cm}$ .

The chemical composition of the groundwater from the active Tíscar and Larva faults is shown on the Piper diagram in Figure 3. The hydrochemical characterization and classification of the water samples allowed us to group them into different families according to the definition of their hydrogeochemical trends, contributing to the assessment of the groundwater circulation model in the studied aquifers. In the cation triangle, the samples are plotted mainly in the left side of the diagram, suggesting  $\text{Ca}^{2+}$  as the predominant element. However, a small group of two samples (15 and 20) lies at the boundary of the  $\text{Mg}^{2+}$  side. Another subgroup of three samples (14, 16, and 17) is plotted mostly in the middle, indicating a mixed water family for the cations. In the anion triangle, the samples are located to the  $\text{HCO}_3^-$  side, indicating bicarbonate as the principal anion. Nevertheless, three samples (12, 17, and 18) are projected on the boundary of the sulphate anion side. A series of water families could be considered, as follows.

##### 3.1.1. $\text{Ca}^{2+}$ - $\text{Mg}^{2+}$ - $\text{HCO}_3^-$ Waters

Most of the samples from the Tíscar and the well (sample 19) from the Larva fault areas can be classified as  $\text{Ca}^{2+}$ - $\text{HCO}_3^-$  and/or  $\text{Mg}^{2+}$ - $\text{HCO}_3^-$ , indicating active recharge, rapid residence time, and temporary hardness. These waters show low salinity, below 9 meq/L, and low-to-moderate electrical conductivity, commonly  $<840 \mu\text{S}/\text{cm}$ , except for samples 13 (Las Gordas spring) and 16 (Gurullas spring), which have conductivities of 1035 and 1311  $\mu\text{S}/\text{cm}$ , respectively. Therefore, these physical–chemical features can be described as an outcome of the incomplete fluid–mineral interaction process occurring in hydrological circuits of moderate depth through Mesozoic carbonate and dolomite rocks.

##### 3.1.2. $\text{Ca}^{2+}$ - $\text{Mg}^{2+}$ - $\text{SO}_4^{2-}$ - $\text{Cl}^-$ Waters

The waters from wells at the Larva fault area (samples 17 and 18) show  $\text{Ca}^{2+}$ - $\text{Mg}^{2+}$ - $\text{SO}_4^{2-}$ - $\text{Cl}^-$  hydrochemical facies with elevated electrical conductivity ( $>840 \mu\text{S}/\text{cm}$ ) and high salinity (up to 30 meq/L). Moreover, there are some samples with high sulfate content, such as 11, 16 ( $>200 \text{ mg/L}$ ), and 17. The enrichment in  $\text{Ca}^{2+}$ ,  $\text{Mg}^{2+}$ ,  $\text{Cl}^-$ , and  $\text{SO}_4^{2-}$  of these waters can be related to the leaching of gypsum- and halite-bearing evaporite formations that outcrop at the Larva area within the Triassic and Miocene stratigraphic sequences. The  $\text{Ca}^{2+}$ - $\text{Mg}^{2+}$ - $\text{SO}_4^{2-}$ - $\text{Cl}^-$  waters from the Tíscar area can also be attributed to local water circulation through gypsum-rich Triassic materials near spring 13. Nevertheless, possible pollution from agricultural practices could influence their high concentration.

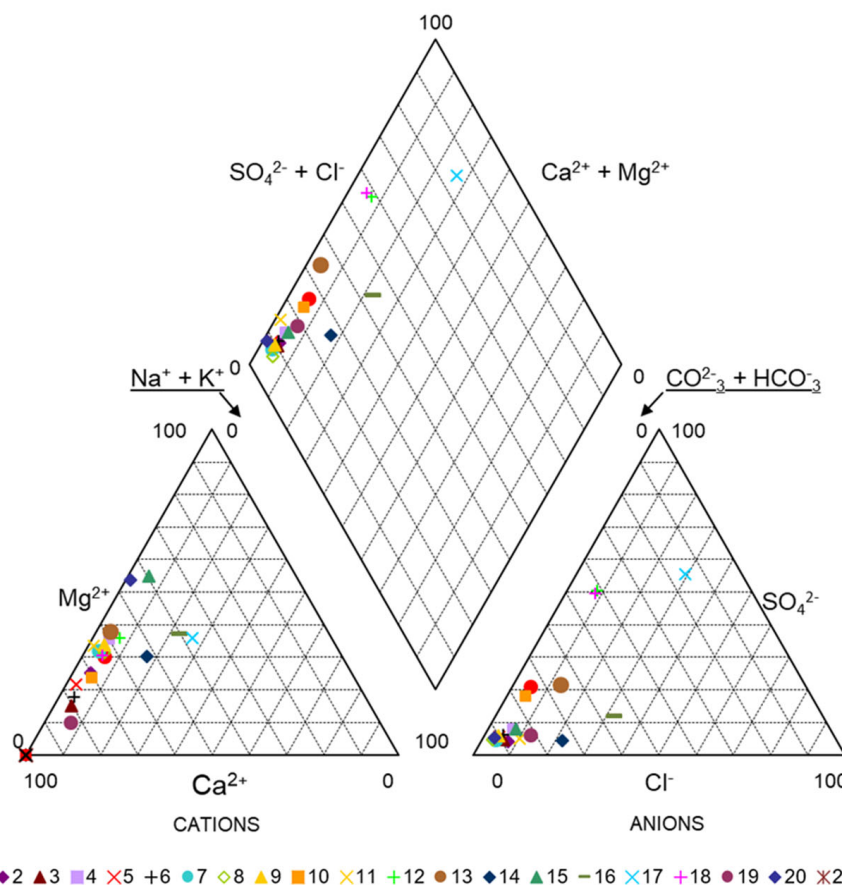


**Figure 3.** Piper diagram showing water geochemistry of groundwater samples.

### 3.1.3. Na<sup>+</sup> Content of the Waters

Two types of relatively Na<sup>+</sup>-rich waters, included in both previously classified groups of waters, can be distinguished at the study area according to their physical–chemical parameters:

- (a) Slightly Na<sup>+</sup>-rich waters and waters enriched in Cl<sup>-</sup>, NO<sub>3</sub><sup>-</sup>, and SO<sub>4</sub><sup>2-</sup> displaying low discharge temperatures (<15 °C) and high salinity (12). This water has a normal or low B content (<0.22 ppm). In groundwaters with low mineralization, the temperature is significantly lower, indicating the possibility of a rapid recharge and shallow flow of infiltrated meteoric waters through carbonate materials [28]. These features, together with the geological position of the sampling sites, suggest that these waters could belong to shallow hydrological paths where interactions with Triassic and/or Miocene evaporites delimiting the aquifers occur. The high level of nitrate also corresponds to waters from sites with intensive olive agricultural activities producing groundwater pollution. The high K contents of these samples could also be due to polluting agricultural activities.
- (b) Na<sup>+</sup>-rich waters enriched in B (>0.33 ppm) with moderate to high exit temperatures (>18 °C) and low to moderate salinity. Groundwaters with a higher temperature in these fault zones are the Acra thermal well (14) at 25.2 °C, Gurullas spring (16) at 20 °C, and Larva well I (17) with a temperature around 25 °C. Considering 20 °C as the hydrothermalism limit [29], this could provide evidence that the origin of some of these waters could be associated with circulation through the active Tíscar and Acra fault zones and, therefore, acquire their temperature from deep zones. Considering that, based on their chemical composition, these groundwaters could appear as immature waters controlled by rock dissolution; the seismic activity in these faults could help to control their physico-chemical properties and the increase in temperature. In addition, these samples exhibit abnormally high traces of boron in

their composition: 0.33 ppm, 0.58 ppm and 0.34 ppm, respectively, the concentration in B in normal groundwater being less than <0.2 ppm. This could indicate the deep circulation of these samples related to the activity of the Tíscar and Larva fault zones. Another potential origin for this abnormal content of boron could be the interaction with evaporite rocks or the effect of agricultural activity [30–32].

### 3.1.4. Tritium Results

The concentration of the radioactive isotope of hydrogen,  ${}^3\text{H}$ , with a half-life of 12.32 years, is measured in tritium units (TUs). Thus, 1 TU is the concentration of one atom in  $10^{18}$  hydrogen atoms. This isotope provides important information to describe the residence time of water in the aquifer, and consequently, the time passed since its infiltration in the 1950s. Thermonuclear tests in the 1950s produced huge inputs of tritium into the atmosphere [33–35].

In the study area, 10 measurements of the tritium concentration were carried out (Table 2) with values between 0.83 and 4.13 TU. Samples 14, 16, and 17 show a tritium concentration below 1.25 TU, indicating that these waters are sub-modern, i.e., they are waters that were recharged before 1952, without the input of precipitation after pumping the aquifers. Sample 7 presents a tritium concentration somewhat bigger than that of 2; therefore, it could be a more ancient water but one that has been affected slightly by modern input waters. Groundwaters with concentrations below 1 TU are mostly dated prior to 1940 [36]. Moreover, samples 1, 3, 5, 9, 11, and 24 feature concentrations of this radioactive isotope above 2 TU, which may be indicative a mix between modern and sub-recently recharged waters (5–10 years). However, these waters have a high uncertainty, indicating both the presence of infiltration water from the early 1950s and recently infiltrated waters, with a rapid turnover and low residence time in the aquifer.

### 3.2. Groundwater Origins

The physical–chemical parameters of the waters from the Tíscar and Larva areas suggest that thermal and cold water sources are present in the groundwaters of the studied area. Cold waters from low-depth aquifers are not commonly in equilibrium with the host rocks, whereas high-temperature waters tend to be equilibrated with the reservoir materials, depending on several variables, such as the time of interaction or the mineral composition of the rocks. During the uprise of deep waters along the faults, in which is mixes with cold groundwaters and undergoes ion exchange processes due to rock–water interactions, important changes in the water's chemical composition could occur, leading to the inability to determine a clear origin of the water samples and their equilibrium temperature. At the study area, the high  $\text{Na}^+$  and B content and high  $\text{Na}^+/\text{K}^+$  of these waters could indicate that these waters have the highest level of equilibrium with the original deep aquifer material, whereas for the rest of the collected samples, the waters were re-equilibrated with other materials or mixed with shallow fluids during its rise to the surface. Dogdu and Bayari [37] and Forrest et al. [32] found that the mixing of shallow waters with hydrothermal fluids results in a higher electrical conductivity, warmer temperatures, and elevated concentrations of Na, Cl, Fe, Li, B, Br, Mn, Al, I, and As, which agrees with what was observed in the investigated samples from Larva and Tíscar.

Consequently, this study of groundwaters could reveal the existence of heating processes that have affected deep aquifers. The absence of the uprising of magmatic bodies at a shallow depth in the studied area indicates that the investigated  $\text{Ca}^{2+}\text{-Mg}^{2+}\text{-SO}_4^{2-}\text{-Cl}^-$  groundwaters with an elevated electrical conductivity (commonly  $>840 \mu\text{S}/\text{cm}$ ), high salinity (up to 30 meq/L), higher temperatures ( $>20^\circ\text{C}$ ), and significant traces of boron in their composition could be formed by deep water circulation (up to 4–6 Km) through the highly permeable conducts of local faults. Water upflow through the Tíscar and Larva fault zones could have caused cooling and fluid–rock interaction processes which modified the original features of the waters.

Considering that the entire hydrological path depends on the material's permeability, chemical properties are likewise sensitive to changes in permeability related to fault activity [29]. In order to detect changes in water composition and behavior after seismic events, i.e., [38–40] a periodic study of selected sites of sampling was carried out. No important variations in the physical–chemical parameters were observed. The only significant change was a slight increase in the EC of sample 19 (Larva Well I) that could be connected with the recent seismic event in Peal de Becerro (September 18, 2014) with a magnitude of 2.8, several days prior to the periodical study.

The tritium analyses suggest that the time since the infiltration of water with less than 0.75 TU is more than 50 years. These water samples correspond to some samples with abnormal elevated temperatures and trace boron content, which hint at the idea of ancient and deep waters.

### 3.3. Geochemical Modeling: Saturation Indices

Saturation indices (SIs) were used to perform geochemical modelling. The SIs were calculated according to the model of hydrochemical equilibrium, created using the PHREEQC version 2 software [41]. This software is based on the equilibrium of aqueous fluid chemistry interacting with other solid or gaseous phases according to the ion-association aqueous model to calculate speciation and SIs. SIs show the degree of chemical equilibrium between aqueous solutions and minerals in the aquifer host material, providing the degree of the processes of crystallization and/or dissolution due to the mineral–fluid interaction.

The calculations are based on the relation between the ion activity product (IAP) and the constant of temperature equilibrium (KT):  $SI = \log(IAP/KT)$ . SIs specify the substances that might crystallize and the phases that could be dissolved in water [42,43].

An  $SI < 0$  means that the solid phase (mineral) is not saturated (undersaturated) regarding water, so it will be disposed to dissolve until the balance is reached. Mineral precipitation could occur when  $SI > 0$ , representing a condition of oversaturation.

Figure 4 shows the SIs obtained for Ca-montmorillonite, kaolinite, illite, gypsum, halite, calcite, and dolomite. The SIs for calcite and dolomite revealed that most of the studied waters are oversaturated or near to equilibrium with these carbonates, indicating the possible precipitation of these minerals. Nevertheless, samples 1 (Rosales spring), 22 (Bernardo spring), and 23 (Collados well) are slightly undersaturated for these carbonate minerals, allowing for the potential dissolution of these minerals. The high degree of undersaturation with respect to halite and gypsum in most of the samples means the dissolution of these minerals is possible, enriching the groundwater in  $\text{Na}^+$ ,  $\text{Ca}^{2+}$ ,  $\text{Cl}^-$ , and  $\text{SO}_4^{2-}$ . Accordingly, groundwater could derive from a gypsum- and halite-poor environment, or, even, the aquifer permanence time might be short, with no time for water–rock interaction process mechanisms. This evident evaporite mineral undersaturation suggests a potential evaporitic material dissolution input in the waters from these fault areas [44,45]. In relation to clay minerals (kaolinite, montmorillonite, and illite), waters from the Tíscar waterfall (4) and from the San Sebastian spring in Quesada (11) are oversaturated with these minerals, indicating a possible precipitation of clay minerals in these waters. In contrast, the waters from the Cueva del Agua spring (8) and the Belerda spring (10) are subsaturated in these clay minerals; therefore, the dissolution of these minerals might be possible. The samples from the Higueral spring (2), Church Huesa spring (3), Carboneras spring (5), and Candilejo spring (7) are close to equilibrium in relation to clays. PHREEQC did not calculate the SI for the samples from the Rosales spring (1), Vadillo 3 Caños spring (6) and Don Pedro spring (9) due to the very low content of Si and Al, which could suggest no precipitation and dissolution for these minerals.

The saturation indices for the samples with a high temperature and abnormal boron content (14, 16, and 17) are near to equilibrium for Ca-Mg carbonates (calcite and dolomite) and suggests oversaturation with clay minerals (smectite, illite, and kaolinite). This could favor the precipitation of these minerals while the dissolution of evaporites is occurring. The samples from locations 12, 13, 15, and 18–23 are also saturated for clay minerals.

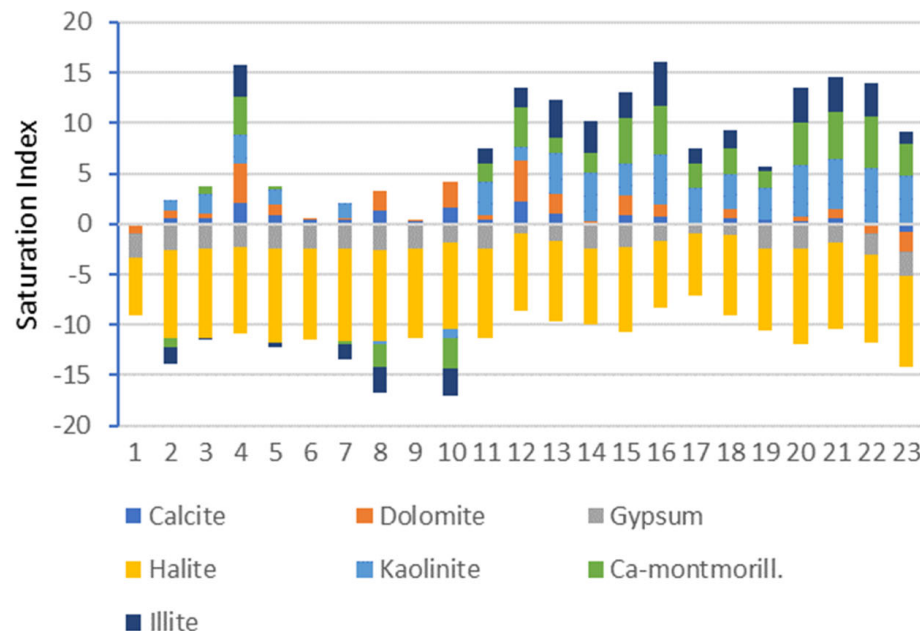


**Figure 4.** Saturation indices of Tíscar–Larva fault zone groundwater samples.

### 3.4. Aluminosilicate Stability

Given that the crystallization of clay minerals can control fault dynamics due to their low-friction behavior, aqueous activity diagrams of the  $\text{SiO}_2\text{-Al}_2\text{O}_3\text{-Na}_2\text{O}\text{-H}_2\text{O}$  and  $\text{SiO}_2\text{-Al}_2\text{O}_3\text{-CaO}\text{-H}_2\text{O}$  systems were assembled in order to assess the stability of clay minerals relative to other aluminosilicate phases (see Figure 5). Hem [46] indicated that mineral and groundwater reactivity depends on the proton ( $\text{H}^+$ ) availability, the time of residence, and the contact surface. Mineral stability diagrams show the importance of dissolution and the relationships between primary and clay minerals in an aqueous environment [47]. The Y-axis shows the  $\log ([\text{cation}^{n+}] / [\text{H}^+]^n)$  and shows that the charge of the cations that are released has to be balanced by  $\text{H}^+$  consumption [41]. In addition, it was assumed that the solid phase and end member compositions conserve Al, which allows them to obviate it. The diagrams were made according to the equilibrium assumptions in Tardy [48] (for 25 °C, 1 atmosphere) that assumed coarsely represented sampled groundwater conditions [43]. In Figure 5A, the stability fields for albite, gibbsite, kaolinite, and Na-montmorillonite are represented as a function of  $\log ([\text{Na}^+] / [\text{H}^+])$  and  $\log [\text{H}_4\text{SiO}_4]$ , where [] means solute activity computed for PHREEQC [49]. Figure 5B contains the stability fields for the anorthite, gibbsite, kaolinite, and Ca-montmorillonite, represented as a function of  $\log ([\text{Ca}^{2+}] / [\text{H}^+]^2)$  and  $\log [\text{H}_4\text{SiO}_4]$  [41]. These diagrams show how the water–mineral equilibrium for the groundwater in this area of study is represented in both the stability diagrams around the boundary of kaolinite/smectite (montmorillonite and Na-Ca-montmorillonite) stability. Moreover, all the samples are above the saturation equilibrium of quartz.

### 3.5. Mineral and Petrographic Characterization of the Fault Rocks

The XRD, SEM, and TEM-AEM characterization of the materials across the zone of damage of the fault zones related to the groundwater sites revealed evidence of deep-water circulation. These analyses were carried out in order to identify the presence or absence of thermodynamically stable minerals suggested by the PHREEQC results, as well as to clarify the textural disposition of these authigenic minerals produced during fluid–rock interaction processes.

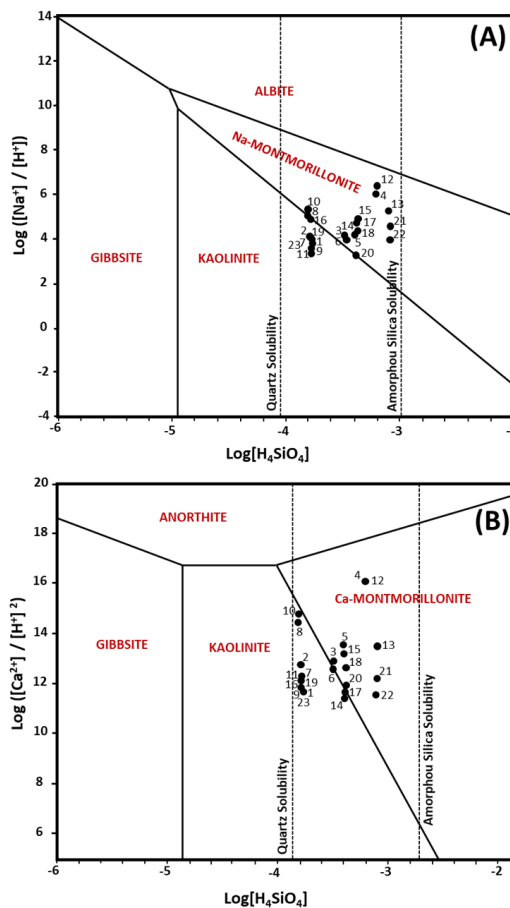


**Figure 5.** Mineral stability diagrams. (A)  $\text{SiO}_2 - \text{Al}_2\text{O}_3 - \text{Na}_2\text{O} - \text{H}_2\text{O}$  system. (B)  $\text{SiO}_2 - \text{Al}_2\text{O}_3 - \text{CaO} - \text{H}_2\text{O}$  system. Numbers represent the labels of the studied samples.

Based on the lithologic/structural features, the samples can be classified as coarse-grained cataclasites and foliated fault gouges. Deformation is preferentially concentrated in the marly rocks, although surfaces with a well-polished surface and striae are very common in carbonate rocks (Figure 6).

The XRD data indicate that the main mineral association of the undamaged rocks is between calcite and mica (Figure 7). Quartz and feldspars are present in small amounts. The mica presence is revealed by a narrow 001 peak sat at  $10 \text{ \AA}$  in the XRD pattern. Heating and ethylene glycol solvation treatments do not modify this peak, which suggests that expandable layers are not present. The SEM images show that the grain size in all the carbonate-rich rocks is medium to coarse (Figure 8A). These rocks are poorly sorted.

In spite of the mineral association strongly depending on the original protolith composition, fault-damaged rocks are enriched in phyllosilicates, with the amount of mica, in particular, increased (Figure 9A).

In the fault rocks associated with sites with  $\text{Na}^+$ -rich waters probably equilibrated with deep aquifers, a small amount of smectite was detected in the XRD diagrams, seen in its  $14.5 \text{ \AA}$  spacing expanding to  $16.9 \text{ \AA}$  after ethylene glycol treatment. Cross-cutting veins commonly filled with large dolomite and calcite crystals were frequently observed in fault rocks sampled at these sites (Figure 8B). The EDX microanalyses revealed that large carbonate grains within the veins are rich in Si and Al, suggesting the presence of very-small-sized silicate inclusions. The SEM images also reveal that the strain distribution is irregular. High-strain zones can be separately recognized, with bands developed through foliation caused by clay mineral enrichment. The SEM images also show that the internal architecture of the deformed materials is made of oriented mica-rich lenses juxtaposed to the predominant carbonate bands, which are apparently undeformed (Figure 9A,B).

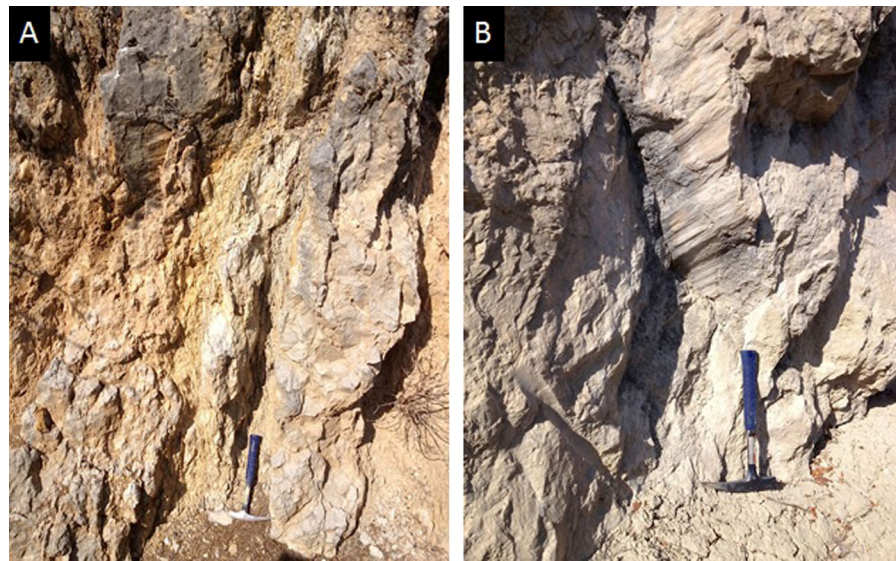


**Figure 6.** Fault rocks from the damage zone of the Tíscar and Larva fault areas. (A) Foliated fault gouge in marly rocks of the Tíscar fault zone. (B) Polished and striated surface in carbonate rocks (Larva fault).

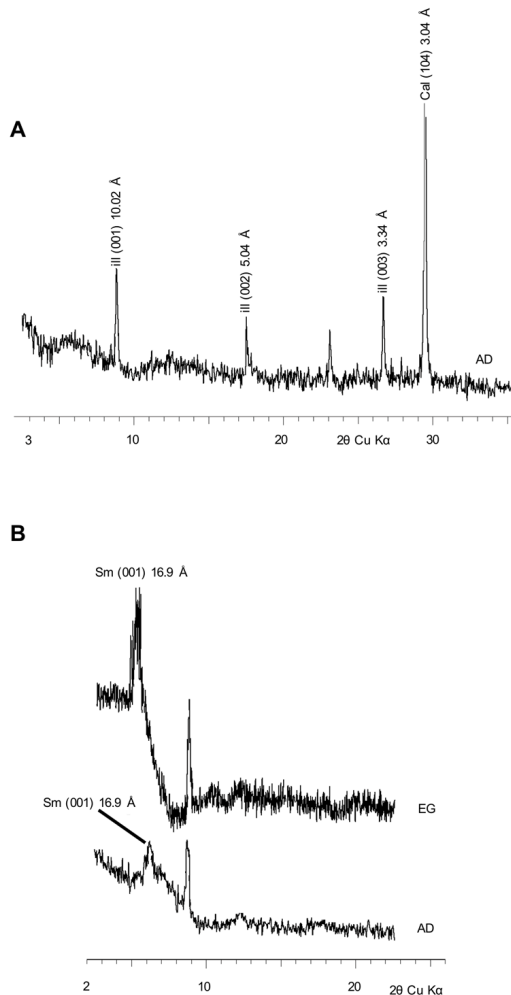


**Figure 7.** (A) XRD diagram of undamaged samples. (B) XRD diagrams of damaged rocks bearing slip surfaces with crystallization of smectite. AD: Air-dried sample. EG: Sample in ethylene glycol. Ms: mica. Sm: smectite. Cal: calcite.

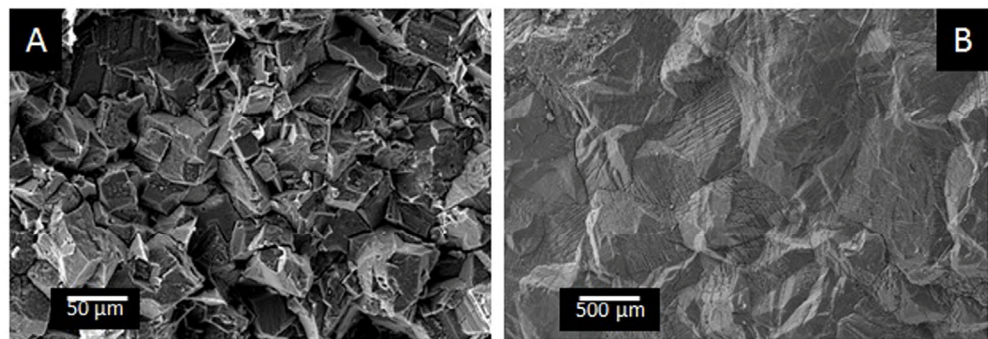


**Figure 8.** (A) SEM image of a non-deformed medium- to coarse-grained carbonate-rich rock. (B) Cross-cutting vein in fault rock filled with dolomite and calcite crystals.

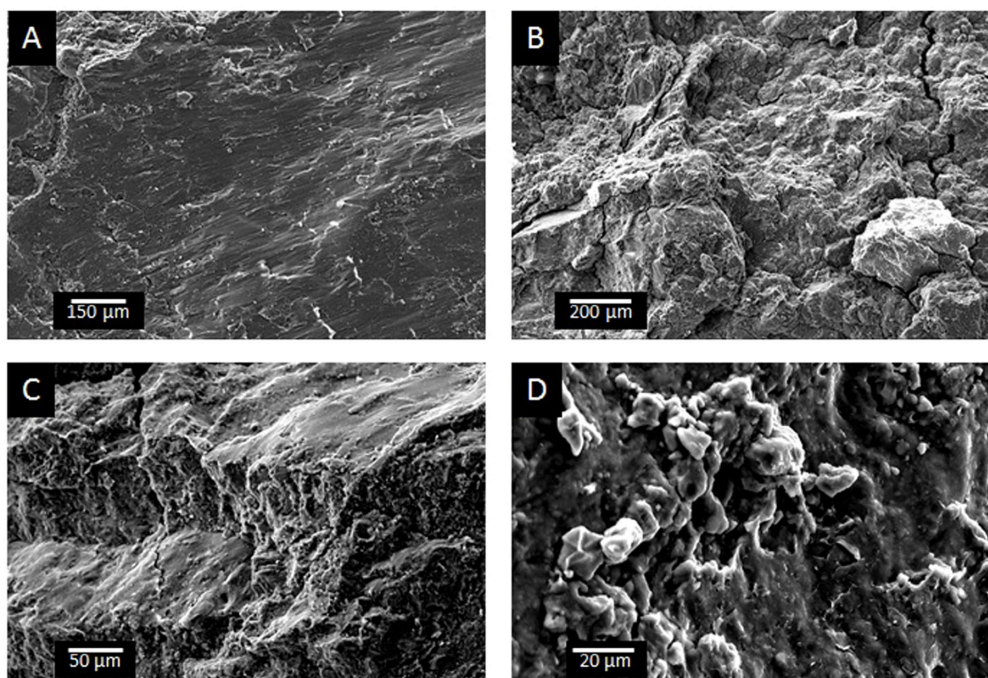


**Figure 9.** (A) Mica-rich high-strain band in a fault rock. (B) Network of slip surfaces among apparently undeformed carbonate bands. (C) Thin films of smectite that have grown on the fracture surfaces. (D) Flakes of smectite crystallized on a slip surface.

A network of slip surfaces can be observed in these materials. However, no evidence of neoformation for this mineral was found in the fault rocks and its concentration seems to be related with the reorientation of inherited crystals and clay smearing processes associated with fault deformation. However, smectite appears in the SEM images as thin films that have grown on the fracture surfaces (Figure 9C). Compositionally (Table 3), the AEM analyses reveal an Al-rich dioctahedral smectite composition (from 1.50 to 1.96 a.p.f.u. in the octahedral sheet).

Tectonic and fluid circulation can affect the generation and enrichment of clays in fault zones [12]. Mineral processes associated with cataclasis and fluid infiltration can exhibit an important role in producing appropriate microenvironments favoring the nucleation of new minerals. In fault zones, the reason why a mineral assemblage crystallizes depends not only on the temperature but also on the elemental composition of the fluids reacting with the protolith and the crystallization mechanism [50,51]. Clay minerals can replace previous minerals or can be formed by direct precipitation from fluids circulating in the area [52,53]. The concentration and circulation of fluids in the microstructures of fault rocks, even under very low temperatures, can promote the neoformation of clays by processes of structural

diagenesis [7,54]. In the study zone, the As, Be, Si, Mg, and B groundwater enrichment in certain samples (thermal Acra well (14), Gurullas well (16) and Larva well I (17)), as well as the high temperature of the groundwater discharged from these wells, can be related to the presence of smectitic minerals as a typical pattern of changes produced by fluid–rock low-temperature interaction with the subsequent precipitation of authigenic minerals. Therefore, the presence of smectite and cross-cutting veins filled with dolomite (Figure 8B) suggests that recurrent inputs of fluids circulating through the fault were responsible for the alteration pattern of the fault rocks. The chemical composition of the waters in rock pores affects the precipitation of neoformed clays in fault zones [12,55]. The precipitation of dolomite in veins can be used as an indicator of the high salinity of the fluids circulating in fault rocks [7,56].

**Table 3.** Structural formulae for representative smectites from fault rocks normalized to  $O_{10}(OH)_2$  on the basis of AEM data.

	Si	AlIV	AlVI	Fe	Mg	$\Sigma$ Oct.	Ca	K	Na	$\Sigma$ Inter.
EG-4-1	3.99	0.01	1.63	0.21	0.30	2.14	0.02	0.07	0.00	0.09
EG-4-2	3.96	0.04	1.50	0.35	0.36	2.21	0.00	0.05	0.00	0.05
EG-6-1	3.65	0.35	1.96	0.12	0.07	2.15	0.00	0.07	0.00	0.07
EG-6-2	3.72	0.28	1.55	0.30	0.29	2.14	0.00	0.26	0.20	0.46
EG-7-1	3.90	0.10	1.68	0.22	0.22	2.12	0.03	0.12	0.00	0.15
EG-7-2	3.92	0.08	1.63	0.23	0.22	2.08	0.00	0.30	0.00	0.30

Hence, regarding clay minerals, the presence of smectite was in good agreement with the PHREEQC output. Although PHREEQC predicted that kaolinite would be thermodynamically favored for mineral precipitation in the aquifer, this mineral was not observed in the rock samples. The presence of some of the calculated points in the kaolinite field in Figure 5, always very near to the montmorillonite field, can be explained by taking into account that the presented diagrams cannot consider two important chemical parameters of the relationships between kaolinite and smectite: the Al/Si ratio and the presence of K as the most abundant interlayer cation of smectite in general, e.g., [57] and also in this particular case (Table 3). Therefore, the diagrams are designed, according to the traditional point of view, for  $Ca^{2+}$  and  $Na^+$  as interlayer cations, but they are almost absent in the studied smectites.

Instead, smectite was found to be the main authigenic clay mineral at the fault gouges. The presence of inherited mica crystals can act as nucleation sites for smectite. High-salinity waters in restricted environments can accelerate mineral authigenesis processes [58]. The flow of fluids controlled by tectonics can produce high-salinity microenvironments facilitating changes in the mica octahedral layer charge that favor its transformation and the neoformation of clay minerals [59–61]. Abad et al. [54] described smectite neoformation during a low-temperature stage in the Padul fault.

### 3.6. Effect of Authigenic Minerals on Mechanical Behavior

The electron microscopy study of the studied fault rocks has shown that smectite micro-scale precipitations are abundant within fault rocks in the study area, producing carbonate microblocks frequently coated with clay minerals. This suggests that under brittle conditions, smectite crystallization on slip surfaces favors the creep deformation of faults.

The behavior of fault zones is strongly influenced by clay minerals, which control permeability and frictional properties [62]. Thus, phyllosilicates can exhibit a great influence on the weakening of faults. Soft clays in fault gouges with foliation are very important in active creeping sections of faults. Ikari et al. [63] showed that the friction behavior of smectite-rich fault rocks developed in different geological conditions depends on the amount of water, provided stress, phyllosilicate enrichment, and gliding speed. Sakuma et al. [64] have shown that the presence of smectite can intensely decrease the crustal fault

strength that favors creeping processes. Localized fluid circulation and stress-induced dissolution–precipitation can explain the presence of the network of slip surfaces coated with smectite in the Tíscar samples (Figure 9D), which favors their physical weakening. This mechanism of deformation has been proposed for some San Andreas Fault segments, where creeping is predominant [65–67]. In the Tíscar area, the formation of this hydrothermal smectite, with an appropriately small frictional strength ( $\mu \leq 0.2$ ) [68], contributed to the weakening of the original carbonate-rich material of the protolith and to the favoring of the creep behavior in the fault.

Therefore, we consider that newly crystallized smectite under conditions of localized fluid flow on displacement surfaces joining carbonate micro blocks at the fault rocks of the Tíscar fault area controlled brittle fault behavior favoring weakening and creeping processes.

#### 4. Conclusions

In the Larva and Tíscar fault zones, the groundwater hydrochemistry, geochemical modeling, and geochemical processes identified, and the mineralogical and petrographic evidence of the presence of clay minerals and their distribution allow for the following conclusions to be drawn. The results could also probably be useful and relevant to future studies of fault zones:

1. Saline waters (up to 30 meq/L) rich in  $\text{Ca}^{2+}$ - $\text{Mg}$ - $\text{SO}_4^{2-}$ - $\text{Cl}^-$ , with elevated conductivity (frequently  $> 840 \mu\text{S}/\text{cm}$ ), higher temperatures ( $> 20^\circ\text{C}$ ) and noteworthy boron contents are associated with deep groundwater flow through the Tíscar and Larva fault zones.
2. The PHREEQC geochemical modeling output suggests that Na and Ca-montmorillonite and kaolinite are clay minerals likely to be precipitated from waters from these sites.
3. The prediction of the thermodynamic state using PHREEQC was accurate, with the exception of kaolinite. The presence of smectite in the fault gouges was identified through XRD, SEM, and TEM-AEM data. Inherited illite crystals acting as nucleation sites for the newly formed smectite and the influence of  $\text{Ca}^{2+}$  and Na from groundwater on the preferential stabilization of smectite are some of the factors that could impede kaolinite crystallization.
4. Thin films of neoformed smectite and cross-cutting veins of calcite and dolomite are related to fragile deformation and mineral–thermal–fluid interaction. Therefore, deformation and groundwater circulation promoted the creation of microenvironments where the nucleation of new minerals cover displacement surfaces. Clays lubricated the carbonate rock fragments, which favors creeping over stick-slip deformation.
5. Hydrochemical, isotopic, and mineralogical data from the Tíscar and Larva fault zones can help to select locations where groundwater physico-chemical properties and composition can suggest tectonic fault activity. Thus, the locations characterized by an elevated water temperature and significant boron content (i.e., Acra 14, Gurullas 16, Larva 17) can be considered indicators of deep water flow triggered by the Tíscar and Larva fault zones. These locations should be specially monitored to provide warnings of earthquake activity.

**Author Contributions:** Conceptualization, R.J.-E., P.H.-P. and J.J.-M.; methodology, R.J.-E., P.H.-P. and J.J.-M.; investigation, R.J.-E., P.H.-P. and J.J.-M.; resources, R.J.-E. and J.J.-M.; writing—original draft preparation, R.J.-E., P.H.-P. and J.J.-M.; writing—review and editing, R.J.-E., P.H.-P. and J.J.-M.; supervision, R.J.-E. and J.J.-M.; funding acquisition, R.J.-E. and J.J.-M. All authors have read and agreed to the published version of the manuscript. R.J.-E. and P.H.-P. obtained and interpreted the groundwater data and performed the geochemical modeling. J.J.-M. is responsible for the XRD, SEM, and TEM studies of the fault rocks. All authors contributed to the writing of the paper.

**Funding:** Financial support has been supplied by the Research Group RNM-325 of the Junta de Andalucía (Spain).

**Data Availability Statement:** The raw data supporting the conclusions of this article will be made available by the authors on request.

**Conflicts of Interest:** The authors declare no conflicts of interest.

## References

1. Gudmundsson, A. Active Fault Zones and Groundwater Flow. *Geophys. Res. Lett.* **2000**, *27*, 2993–2996. [[CrossRef](#)]
2. Rosen, M.R.; Binda, G.; Archer, C.; Pozzi, A.; Michetti, A.M.; Noble, P.J. Mechanisms of Earthquake-Induced Chemical and Fluid Transport to Carbonate Groundwater Springs after Earthquakes. *Water Resour. Res.* **2018**, *54*, 5225–5244. [[CrossRef](#)]
3. Fronzi, D.; Mirabella, F.; Cardellini, C.; Caliro, S.; Palpacelli, S.; Cambi, C. The Role of Faults in Groundwater Circulation before and after Seismic Events: Insights from Tracers, Water Isotopes and Geochemistry. *Water* **2021**, *13*, 1499. [[CrossRef](#)]
4. Caine, J.S.; Minor, S.A. Structural and geochemical characteristics of faulted sediments and inferences on the role of water in deformation, Rio Grande Rift, New Mexico. *Geol. Soc. Am. Bull.* **2009**, *121*, 1325–1340. [[CrossRef](#)]
5. Chitsazan, M.; Manshadi, B.D. Role of Mehriz Fault in hydrochemical evolution and groundwater flow of Yazd aquifer, central Iran. *Arab. J. Geosci.* **2021**, *14*, 560. [[CrossRef](#)]
6. Mammoliti, E.; Fronzi, D.; Cambi, C.; Mirabella, F.; Cardellini, C.; Patacchiola, E.; Tazioli, A.; Caliro, S.; Valigi, D. A Holistic Approach to Study Groundwater-Surface Water Modifications Induced by Strong Earthquakes: The Case of Campiano Catchment (Central Italy). *Hydrology* **2022**, *9*, 97. [[CrossRef](#)]
7. Jiménez-Millán, J.; Abad, I.; García-Tortosa, F.J.; Jiménez-Espinosa, R. Structural Diagenesis in Clay Smearing Bands Developed on Plio-Pleistocene Sediments Affected by the Baza Fault (S Spain). *Minerals* **2022**, *12*, 1255. [[CrossRef](#)]
8. Bousquet, R.; Vidal, O.; de Capitani, C. Metamorphic reactions, fluids release and their influence on subduction earthquakes. *Geophys. Res. Abstr.* **2009**, *11*, EGU2009–EGU12554.
9. Vidal, O.; Dubacq, B. Thermodynamic modelling of clay dehydration, stability and compositional evolution with temperature, pressure and H<sub>2</sub>O activity. *Geochim. Cosmochim. Acta* **2009**, *73*, 6544–6564. [[CrossRef](#)]
10. Sánchez-Roa, C.; Vidal, O.; Jiménez-Millán, J.; Nieto, F.; Faulkner, D.R. Implications of sepiolite dehydration for earthquake nucleation in the Galera Fault Zone: A thermodynamic approach. *Appl. Geochem.* **2018**, *89*, 219–228. [[CrossRef](#)]
11. Beynon, S.J.; Faulkner, D.R. Dry, damp, or drenched? The effect of water saturation on the frictional properties of clay fault gouges. *J. Struct. Geol.* **2020**, *140*, 104094.
12. Xu, Z.; Yu, T.; Lin, P.; Li, S. Anomalous patterns of clay minerals in fault zones. *Eng. Geol.* **2023**, *325*, 107279. [[CrossRef](#)]
13. Reddy, D.V.; Nagabhushanam, P. Chemical and isotopic seismic precursory signatures in deep groundwater: Cause and effect. *Appl. Geochem.* **2012**, *27*, 2348–2355. [[CrossRef](#)]
14. Moore, D.E.; Rymer, M.J. Talc-bearing serpentinite and the creeping section of the San Andreas fault. *Nature* **2007**, *448*, 795–797. [[CrossRef](#)] [[PubMed](#)]
15. Moore, D.E.; Lockner, D. Friction of the Smectite Clay Montmorillonite: A Review and Interpretation of Data. In *The Seismogenic Zone of Subduction Thrust Faults*; Dixon, T.H., Moore, C., Eds.; Columbia University Press: Chichester, NY, USA, 2007; pp. 317–345.
16. Tendero-Salmerón, V.; Galindo-Zaldívar, J.; Pelaez, J.A.; Martínez-Martos, M.; Henares, J.; Marín-Lechado, C.; López-Garrido, A.C. Seismicity in strike-slip foreland faults (central Betic cordillera front): Evidence of indentation tectonics. *Tectonics* **2020**, *39*, e2020TC006143. [[CrossRef](#)]
17. Sanz de Galdeano, C.; Galindo-Zaldívar, J.; López-Garrido, A.C.; Alfaro, P.; Pérez-Valera, F.; Pérez-López, A.; García-Tortosa, F. La falla de Tíscar: Su significado en la terminación sudoeste del Arco Prebético. *Rev. Soc. Geol. España* **2006**, *19*, 271–280.
18. Foucault, A. Étude Géologique des Environs des Sources du Guadalquivir (prov. Jaén et Grenade, Espagne Méridionale). Ph.D. Thesis, Université de Paris VI, Paris, France, 1971; 633p.
19. Moral, F.; Balanyá, J.C. Recent fault-controlled glaci deformation and its role in the fluvial capture of the Guadix-Baza basin (Betic Cordillera, southern Spain). *Geomorphology* **2020**, *363*, 107226. [[CrossRef](#)]
20. Frizon de Lamotte, D.; Andriem, J.; Guezou, J.C. Cinématique des chevauchements néogènes dans l’Arc bético-rifain: Discussion sur les modèles géodynamiques. *Bull. Soc. Géol. France* **1991**, *162*, 611–626. [[CrossRef](#)]
21. Sanz de Galdeano, C. Presencia de estructuras oblicuas en el sector central del Subbético y significado de la falla de Tíscar (Cordillera Bética). *Rev. Soc. Geol. España* **2003**, *16*, 103–110.
22. Sanz de Galdeano, C.; Peláez, J.A. *Fallas Activas en la Cordillera Bética. Una Aproximación a Partir de la Información Tectónica y Sísmica*; University of Granada: Granada, Spain, 2011; 287p.
23. Sanz de Galdeano, C.; García Tortosa, F.J.; Peláez, J.A. Estructura del Prebético de Jaén (sector de Bedmar). Su relación con el avance del subbético y con fallas en el basamento. *Rev. Soc. Geol. España* **2013**, *26*, 55–68.
24. Pérez-Valera, F.; Sánchez-Gómez, M.; Peláez, J.A.; Pérez-Valera, L.A. Fallas de edad Pleistoceno superior en el entorno del terremoto de Huesa, Jaén (4.4 mbLg, 31/01/2012): Implicaciones sismotectónicas. *Geogaceta* **2012**, *52*, 25–28.
25. ITGE. *Atlas Hidrogeológico de la Provincia de Jaén*; Instituto Tecnológico Geominero de España, Diputación Provincial de Jaén: Jaén, Spain, 1997; ISBN 8489560234.
26. ITGE. *Atlas Hidrogeológico de Andalucía*; Instituto Tecnológico Geominero de España, Junta de Andalucía: Madrid, Spain, 1998; ISBN 8478403515.
27. Nieto, F.; Ortega-Huertas, M.; Peacor, D.R.; Aróstegui, J. Evolution of illite/smectite from early diagenesis through incipient metamorphism in sediments of the Basque-Cantabrian Basin. *Clays Clay Miner.* **1996**, *44*, 304–323. [[CrossRef](#)]

28. Marques, J.M.; Carreira, P.M.; Carreira, J.M.; Espinha Marques, J.M.; Chaminé, H.I.; Fonseca, P.E.; Monteiro Santos, F.A.; Eggenkamp, H.G.M.; Teixeira, J.A. The role of geosciences in the assessment of low-temperature geothermal resources (N-Portugal): A review. *Geosci. J.* **2010**, *14*, 423–442. [[CrossRef](#)]
29. Italiano, F.; Bonfanti, P.; Pizzino, L.; Quattrocchi, F. Geochemistry of fluids discharged over the seismic area of the Southern Apennines (Calabria region, Southern Italy): Implications for Fluid-Fault relationships. *Appl. Geochem.* **2010**, *25*, 540–554. [[CrossRef](#)]
30. Yuce, G. A geochemical study of the groundwater in the Misli basin and environmental implications. *Environ. Geol.* **2007**, *51*, 857–868. [[CrossRef](#)]
31. Keskin, T. Groundwater changes in relation to seismic activity: A case study from Eskipazar (Karabuk, Turkey). *Hydrogeol. J.* **2010**, *18*, 1205–1218. [[CrossRef](#)]
32. Forrest, M.J.; Kulongoskib, J.T.; Edwards, M.S.; Farrard, C.D.; Belitzb, K.; Norris, R.D. Hydrothermal contamination of public supply wells in Napa and Sonoma Valleys, California. *Appl. Geochem.* **2013**, *33*, 25–40. [[CrossRef](#)]
33. Clark, I.; Fritz, P. *Environmental Isotopes in Hydrogeology*; Lewis Publishers: New York, NY, USA, 1997; 352p.
34. Hernández-Puentes, P.; Jiménez-Espinosa, R.; Jiménez-Millán, J. Geochemical patterns of groundwater from the Palomares-Carboneras active fault area aquifers (SE Spain): Determination of a network of sensitive sites indicators of seismic events. *Environ. Earth Sci.* **2015**, *73*, 6341–6354. [[CrossRef](#)]
35. Telloli, C.; Rizzo, A.; Salvi, S.; Pozzobon, A.; Marrocchino, E.; Vaccaro, C. Characterization of groundwater recharge through tritium measurements. *Adv. Geosci.* **2022**, *57*, 21–36. [[CrossRef](#)]
36. Custodio, E.; Llamas, M. *Hidrología Subterránea*; Ediciones Omega: Barcelona, Spain, 1983; 2350p.
37. Dogdu, M.S.; Bayari, C.S. Environmental impact of geothermal fluids on surface water, groundwater and streambed sediments in the Akarcay Basin, Turkey. *Environ. Geol.* **2005**, *47*, 325–340. [[CrossRef](#)]
38. Thomas, D. Geochemical precursors to seismic activity. *Pure Appl. Geophys.* **1988**, *126*, 241–266. [[CrossRef](#)]
39. Martinelli, G. Non seismometrical precursors observations in Europe: Steps of earthquake prediction research. In Proceedings of the Workshop Historical Seismic Instruments and Documents: A Heritage of Great Scientific and Cultural Value, Walferdange, Luxembourg, 16–18 May 1994; Conseil de l’Europe, Cahiers du Centre Européenne de Géodinamique et de Séismologie: Bruxelles, Belgium, 1994; Volume 13, pp. 195–216.
40. Toutain, J.P.; Baubron, J.C. Gas geochemistry and seismotectonics: A review. *Tectonophysics* **1999**, *304*, 1–27. [[CrossRef](#)]
41. Appelo, C.A.J.; Postma, D. *Chemical Analysis of Groundwater. Geochemistry, Groundwater and Pollution*; A.A. Balkema: Rotterdam, The Netherlands, 1999; 649p.
42. Drever, J.I. *The Geochemistry of Natural Waters*, 3rd ed.; Prentice-Hall: Upper Saddle River, NJ, USA, 1997; 436p.
43. Kortatsi, B.K. Hydrochemical framework of groundwater in the Ankobra Basin, Ghana. *Aquat. Geochem.* **2007**, *13*, 41–74. [[CrossRef](#)]
44. Singh, C.K.; Rina, K.; Singh, R.P.; Mukherjee, S. Geochemical characterisation and heavy metal contamination of groundwater in Satluj River Basin. *Environ. Earth Sci.* **2014**, *71*, 201–216. [[CrossRef](#)]
45. Cifuentes, G.R.; Jiménez-Espinosa, R.; Quevedo, C.P.; Jiménez-Millán, J. Damming Induced Natural Attenuation of Hydrothermal Waters by Runoff Freshwater Dilution and Sediment Biogeochemical Transformations (Sochagota Lake, Colombia). *Water* **2021**, *13*, 3445. [[CrossRef](#)]
46. Hem, J.D. *Study and Interpretation of Chemical Characteristics of Natural Waters*; Water Supply Paper 2254; US Geological Survey: Washington, DC, USA, 1985.
47. Muñoz, I.; De Andres, A.; Vicente, R. Estabilidad de los minerales de arcilla en las relaciones de interacción arcosas-agua subterránea en el acuífero de Campo Arañuelo. *Geogaceta* **1996**, *20*, 1307–1310.
48. Tardy, Y. Characterisation of the principal weathering types by the geochemistry of waters from European and African crystalline massifs. *Chem. Geol.* **1971**, *7*, 253–271. [[CrossRef](#)]
49. Parkhurst, D.L.; Appelo, C.A.J. *User’s Guide to PHREEQC (Version 2). A Computer Program for Speciation, Batch-Reaction, One-Dimensional Transport, and Inverse Geochemical Calculations*; Water-Resources Investigations Report 99-4259; US Geological Survey: Reston, VA, USA, 1999; 312p.
50. Abad, I.; Jiménez-Millán, J.; Molina, J.M.; Nieto, F.; Vera, J.A. Anomalous reverse zoning of saponite and corrensite caused by contact metamorphism and hydrothermal alteration of marly rocks associated with subvolcanic bodies. *Clays Clay Miner.* **2003**, *5*, 543–554. [[CrossRef](#)]
51. Jiménez-Millán, J.; Velilla, N.; Vázquez, M. Deformation promoted defects and retrograde chloritization of biotite in slates from a shear zone, Southern Iberian Massif, SE Spain. *Clays Clay Miner.* **2007**, *55*, 284–294. [[CrossRef](#)]
52. Jiménez-Millán, J.; Molina, J.M.; Nieto, F.; Nieto, L.M.; Ruiz-Ortiz, P.A. Glauconite and phosphate peloids in Mesozoic carbonate sediments (Eastern Subbetic Zone, Betic Cordilleras, SE Spain). *Clay Miner.* **1998**, *33*, 547–559. [[CrossRef](#)]
53. Leoni, L.; Lezzerini, M.; Battaglia, S.; Cavalcante, F. Corrensite and chlorite-rich C-S mixed layers in sandstones from the Macigno Formation (northwestern Tuscany, Italy). *Clay Miner.* **2010**, *45*, 87–106. [[CrossRef](#)]
54. Abad, I.; Nieto, F.; Reolid, M.; Jiménez-Millán, J. Evidence of phyllosilicate alteration processes and clay mineral neoformation promoted by hydrothermal fluids in the Padul Fault area (Betic Cordillera, SE Spain). *Appl. Clay Sci.* **2022**, *230*, 106669. [[CrossRef](#)]
55. Deocampo, D.M.; Berry, P.A.; Beverly, E.J.; Ashley, G.M.; Jarrett, R.E. Whole-rock geochemistry tracks precessional control of Pleistocene lake salinity at Olduvai Gorge, Tanzania: A record of authigenic clays. *Geology* **2017**, *45*, 683–686. [[CrossRef](#)]

56. Torabi, A.; Jiménez-Millán, J.; Jiménez-Espinosa, R.; García-Tortosa, F.J.; Abad, I.; Ellingsen, T.S.S. Effect of Mineral Processes and Deformation on the Petrophysical Properties of Soft Rocks during Active Faulting. *Minerals* **2020**, *10*, 444. [[CrossRef](#)]
57. Drief, A.; Nieto, F. Chemical composition of smectites formed in clastic sediments. Implications for the smectite-illite transformation. *Clay Miner.* **2000**, *35*, 665–678. [[CrossRef](#)]
58. Cuadros, J.; Andrade, G.; Ferreira, T.O.; de Moya Partiti, C.S.; Cohen, R.; Vidal-Torrado, P. The mangrove reactor: Fast clay transformation and potassium sink. *Appl. Clay Sci.* **2017**, *140*, 50–58. [[CrossRef](#)]
59. Laurich, B.; Urai, J.L.; Vollmer, C.; Nussbaum, C. Deformation mechanisms and evolution of the microstructure of gouge in the Main Fault in Opalinus Clay in the Mont Terri rock laboratory (CH). *Solid Earth* **2018**, *9*, 1–24. [[CrossRef](#)]
60. Clauer, N.; Techer, I.; Nussbaum, C.; Laurich, B. Geochemical signature of paleofluids in microstructures from Main Fault in the Opalinus Clay of the Mont Terri rock laboratory, Switzerland. *Swiss J. Geosc.* **2017**, *110*, 105–128. [[CrossRef](#)]
61. Klee, J.; Potel, S.; Ledésert, B.A.; Hébert, R.L.; Chabani, A.; Barrier, P.; Trullenque, G. Fluid-Rock Interactions in a Paleo-Geothermal Reservoir (Noble Hills Granite, California, USA). Part 1: Granite Pervasive Alteration Processes away from Fracture Zones. *Geosciences* **2021**, *11*, 325. [[CrossRef](#)]
62. Maciel, I.B.; Dettori, A.; Balsamo, F.; Bezerra, F.H.R.; Vieira, M.M.; Nogueira, F.C.C.; Salvioli-Mariani, E.; Sousa, J.A.B. Structural Control on Clay Mineral Authigenesis in Faulted Arkosic Sandstone of the Rio do Peixe Basin, Brazil. *Minerals* **2018**, *8*, 408. [[CrossRef](#)]
63. Ikari, M.; Saffer, D.M.; Marone, C. Frictional and hydrologic properties of clay-rich fault gouge. *J. Geophys. Res.* **2009**, *114*, B05409. [[CrossRef](#)]
64. Sakuma, H.; Lockner, D.A.; Solum, J.; Davatzes, N.C. Friction in clay-bearing faults increases with the ionic radius of interlayer cations. *Commun. Earth Environ.* **2022**, *3*, 116. [[CrossRef](#)]
65. Schleicher, A.M.; van der Pluijm, B.A.; Solum, J.G.; Warr, L.N. Origin and significance of clay-coated fractures in mudrock fragments of the SAFOD borehole (Parkfield, California). *Geophys. Res. Lett.* **2006**, *33*, L16313. [[CrossRef](#)]
66. Schleicher, A.M.; van der Pluijm, B.A.; Warr, L.N. Nanocoatings of clay and creep of the San Andreas fault at Parkfield, California. *Geology* **2010**, *38*, 667–670. [[CrossRef](#)]
67. Schleicher, A.M.; van der Pluijm, B.A.; Warr, L.N. Chlorite-smectite clay minerals and fault behavior: New evidence from the San Andreas Fault Observatory at Depth (SAFOD) core. *Lithosphere* **2012**, *4*, 209–220. [[CrossRef](#)]
68. Behnson, J.; Faulkner, D.R. Frictional strength of sheet silicates under medium to high pressure. *J. Struct. Geol.* **2012**, *42*, 49–61. [[CrossRef](#)]

**Disclaimer/Publisher’s Note:** The statements, opinions and data contained in all publications are solely those of the individual author(s) and contributor(s) and not of MDPI and/or the editor(s). MDPI and/or the editor(s) disclaim responsibility for any injury to people or property resulting from any ideas, methods, instructions or products referred to in the content.